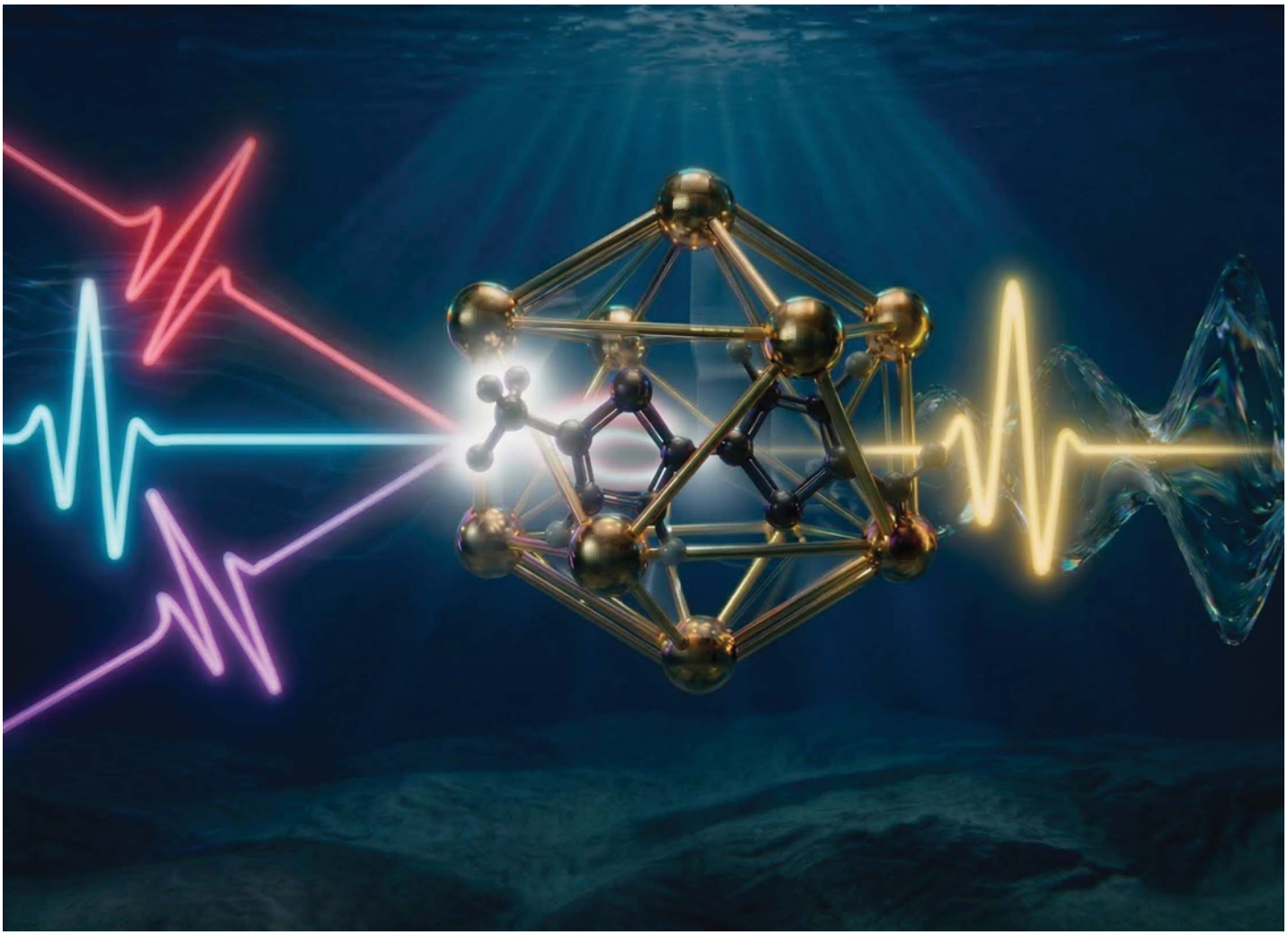

**Showcasing research from Professor Jyotishman Dasgupta's laboratory, Department of Chemical Sciences at Tata Institute of Fundamental Research, Mumbai with collaborative support from Dr Dooshaye Moonshiram (ICMM Madrid).**

Vibrational snapshots of ultrafast C–H bond photoactivation inside a water-soluble nanocage

Photoactivation of C–H bonds in enzyme-like nanocavities can enable diverse photoredox organic transformations in water. Here, we use femtosecond stimulated Raman spectroscopy and transient absorption spectroscopy to probe the structural dynamics of sequential proton-coupled electron transfer, and reveal the role of water in selective C–H functionalization inside a cationic water-soluble nanocage.

Image reproduced by permission of Shashi from *Chem. Sci.,* 2026, **17**, 6390.

Image created with Google Gemini.

## As featured in:


See Sunandita Paul *et al.*, *Chem. Sci.,* 2026, **17**, 6390.

ROYAL SOCIETY OF CHEMISTRY

rsc.li/chemical-science

Registered charity number: 207890

Chemical Science

ROYAL SOCIETY OF CHEMISTRY

EDGE ARTICLE

View Article Online
View Journal | View Issue



Cite this: *Chem. Sci.*, 2026, **17**, 6390

All publication charges for this article have been paid for by the Royal Society of Chemistry

# Vibrational snapshots of ultrafast C–H bond photoactivation inside a water-soluble nanocage

Sunandita Paul,†[a] Shashi,[a] Ankita Das,‡[a] Dooshaye Moonshiram[b] and Jyotishman Dasgupta*[a]

Triggering C–H bond photoactivation reactions inside enzyme-like nanocavities will enable development of green methods to carry out selective organic transformations in water. Recently it was shown that host–guest charge transfer (CT) interactions inside water-soluble cationic nanocages can be used to drive ultrafast C–H bond photoactivation to catalytically form selective products in water *via* a sequential proton-coupled electron transfer (PCET) reaction. However, the primary structural events after light absorption that couple the electron and proton transfer steps during the PCET process have remained elusive, thereby limiting the diversity of cage-confined photoredox catalysis in water. Here we employ structure-sensitive femtosecond stimulated Raman spectroscopy to track the PCET driven catalytic photoactivation of the C–H bond in cage-confined 5-(5-methylthiophene-2-yl)-thiophene-carbaldehyde (BTMC), and its subsequent selective oxidation to the corresponding aldehyde at room temperature in water. Resonance-selective Raman snapshots of the photogenerated radical cation reveal the rich vibrational dynamics of the bithiophene rings leading to formation of a neutral radical at the methyl-carbon site while suggesting kinetic heterogeneity of the deprotonation event. In combination with broadband transient absorption and solvent water kinetic isotope effects, we demonstrate a key role of the pre-organized water cluster around the host–guest complex during C–H bond photoactivation. Our work illustrates the significance of controlling guest self-assembly inside the cage to tune the rate of preorganized proton transfer, and therefore opens a temporal framework for developing universal PCET-guided photoredox transformations in water.

Received 15th July 2025
Accepted 5th February 2026

DOI: 10.1039/d5sc05247e

rsc.li/chemical-science



## Introduction

The most fundamental aspect of any chemical reaction lies in the intricate electronic and structural details of its bond-breaking and/or bond-making steps.[1] It has been a dream of chemists to visualize the nuclear dynamics that drive product formation in well-known organic transformations.[2–6] Selective C–H bond activation[7–9] represents a grand chemistry challenge as it promises to allow atom economy during organic synthesis.[10,11] Classically, C–H activation has been catalytically achieved at metal centers where ligand-to-metal charge transfer interactions (see Fig. 1) play a crucial role in breaking the C–H bond.[12,13] Recently, time-resolved X-ray absorption spectroscopy was used to resolve the orbital-based description of the ligand-to-metal charge transfer interactions.[14] It has been elaborated that such specific and preorganized metal–ligand charge transfer interactions are necessary for widely diverse C–H bond activation reactions.[15]

An alternate way of executing any generic X–H ($X$ = O, N, S or C atom) bond cleavage is through a combination of electron transfer (ET) and proton transfer (PT) steps in pre-organized donor–acceptor systems.[16–18] Confinement of redox complementary organic substrates inside a supramolecular host cavity allows for formation of host–guest donor–acceptor charge transfer interactions[19–25] (Fig. 1). Recently, it was demonstrated that photoexciting such water-soluble host–guest complexes with prominent CT interactions can drive X–H bond-activation chemistry *via* a sequential proton-coupled electron transfer (PCET) mechanism.[24,25] It was hypothesized that the pre-organized water molecules around the supramolecular nanocavities enable O–H and N–H bond cleavage reactions within ~900 fs and ~3 ps respectively, *via* photoinduced PCET.[24] Using this conceptual framework, Das *et al.* reported that ultrafast C–H bond photoactivation within tens of picoseconds could be performed inside a cationic, water-soluble supramolecular host nanocavity.[26] With such a photoredox scheme, the first selective transformation of toluene to benzaldehyde under ambient

[a]*Department of Chemical Sciences, Tata Institute of Fundamental Research, Mumbai, India. E-mail: dasgupta@tifr.res.in*

[b]*Instituto de Ciencia de Materiales de Madrid Consejo Superior de Investigaciones, Científicas Sor Juana Inésde La Cruz 3, Madrid 28049, Spain*

† Current address: Department of Chemistry, The University of Chicago, Chicago, Illinois 60637, USA; and the James Franck Institute, The University of Chicago, Chicago, Illinois 60637, USA.

‡ Current address: School of Chemistry, University of Birmingham, Edgbaston, Birmingham B15 2TT, UK.

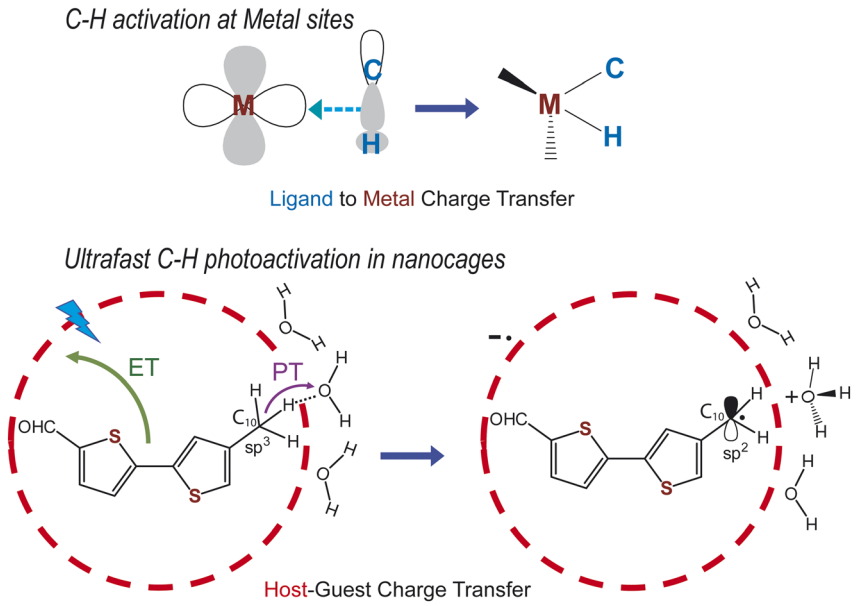


Fig. 1 Conceptual figure depicting C–H activation routes. (top) The traditional C–H bond activation at metal sites; and (bottom) the novel host–guest charge transfer method for ultrafast photoactivation of the C–H bond. The fate of the C–H bond for metal catalyst-based activation is the formation of a metal–carbon bond/complex while for ultrafast photoactivation, a confined C-centered neutral radical is the transient product.

conditions,[26] mimicking the typical enzymatic turnover in water was achieved. However, a clear understanding of all the primary light-induced events, especially the structural dynamics in such a complex nanocavity has remained a critical challenge. More specifically a comprehensive view of the reaction coordinate that drives the sequential photoinduced PCET process has remained elusive. Therefore, it is imperative to watch the non-equilibrium events driving the sequential PCET while providing an experimental test-bed for the theory proposed by Hammes-Schiffer and co-workers[27] on defining a single solvent fluctuation coordinate even for photoinduced PCET reactions.[28] Elucidation of this fundamental reaction coordinate(s) would consequently lead to a rational design principle for a universal scheme of driving PCET-guided photoredox catalysis in water.

Ultrafast vibrational spectroscopy has been used to track structural changes accompanying photoinduced bond breaking steps in many chemical and biological reactions.[29–31] For condensed phase reactions, time-resolved Raman in its variants has been hugely successful due to its selectivity of transient states *via* resonance enhancement.[32] Compelling demonstrations of probing structural dynamics have been shown in diverse reactions such as CT reactions in conjugated polymers,[33–35] photoisomerization reactions in proteins[36,37] and excited state proton transfer reaction in GFP.[38] Additionally, in all these examples, transient Raman spectroscopy enabled watching the reaction coordinate(s) which allowed further tuning of the reaction efficiency of the chemical processes. Herein we use femtosecond stimulated Raman spectroscopy (FSRS)[39] to watch the C–H bond cleavage reaction inside a water-soluble nanocage for the first time, and interrogate the role of the pre-organized water cluster during the sequential photoinduced PCET process.

Substituted thiophenes as well as oligothiophenes of different chain lengths are highly useful for optoelectronic and photodynamic therapy applications although the fundamental organic transformations on the thiophene backbone are challenging due to their enhanced oxidative reactivity of the thiophene rings.[40,41] The paucity of selective C–H activation schemes for converting $-CH_3$ groups on thiophenes to reactive functional groups like aldehydes in one-step at room temperature is rare. To visualize the C–H bond cleavage, we chose 5-(5-methylthiophene-2-yl)-thiophene-carbaldehyde (BTMC) substrate which has a pendant $CH_3$ group (Fig. 1) and confined it inside a water-soluble $Pd_6L_4^{12+}$ nanocavity.[42] Our choice of methyl-substituted bithiophene was therefore to provide a proof-of-concept C–H bond photoactivation reaction while exploiting the large Raman cross-section enabling sensitive visualization of photoinduced structural dynamics. Incarceration of BTMC inside the host nanocage enables the generation of a visible host–guest CT state. Photoexcitation at the CT band triggers the C–H bond photoactivation step through the sequential proton-coupled electron transfer reaction. The whole reaction trajectory was probed in real-time using transient absorption and femtosecond stimulated Raman spectroscopy which captured the radical cation and the neutral radical states through the changes at the C-10 methyl site. The FSRS spectral changes indicate that the proton transfer step occurs from the $C_{10}$–H bond to form a stable C-centred neutral radical, highly conjugated with the bithiophene backbone, and it has an electronic structure that equilibrates with the solvent shell in ~65 ps. The emergence of neutral radical like Raman features as early as tens of picoseconds in the FSRS data provides critical information about the significance of the orientational heterogeneity of the water cluster around the nanocage which drives the C–H

bond photoactivation *via* sequential PCET. Our work, therefore, provides in-depth mechanistic view for the first example of a selective photo-catalytic oxidation of a methyl group to an aldehyde on a thiophene backbone in water under ambient conditions.

## Results and discussion

### Host–guest complexation

The host cationic nanocage $Pd_6L_4^{12+}$ (L = tri-pyridyl-triazine; TPT) was synthesized by following the reported protocols[42] with some modifications (details of the synthesis has been provided in the SI). The nanocage was characterized by carrying out $^1$H-NMR spectroscopy to check the integrity of the self-assembled cage (Fig. S1). We prepared the host–guest complex by mixing 5-equivalents of BTMC in 2.5 mM aqueous solution of the cage (see Fig. 2a) and stirring the solution for 30 minutes. To check the incarceration of BTMC inside the cage, we carried out $^1$H-NMR spectroscopy after filtering the excess guest from the yellow-coloured solution. Fig. 2b shows the NMR spectra of BTMC⊂Cage in $D_2O$. The peak marked in green arises from the molecule inside the cage while the cage protons (assignment in SI Fig. S1) are marked in red. We see that all the guest protons are upfield shifted inside the cavity as compared to the free molecule $^1$H NMR spectra in $CDCl_3$ (Fig. S2). The $-CH_3$ proton in BTMC⊂Cage appears at 1.26 ppm as compared to 2.51 ppm in free BTMC in $CDCl_3$. The unequivocal upfield shift can only be explained by the shielding effect of the cavity on the molecule. $^1$H NMR binding titration was performed to study the host–guest complexation behaviour between the host cage and BTMC guest. Increasing amounts of BTMC were added to 2.5 mM cage in $D_2O$, and the $^1$H NMR spectra were recorded. Slight changes in chemical shift values were seen for the cage aromatic protons. Relative peak area integration of both host and guest protons indicated complex formation in 1 : 1 stoichiometry, as shown in Fig. S3 and S4.

Steady-state absorption measurements were conducted to characterize the optical features of the host–guest complex. Fig. 2c shows the absorption of the cage (black trace), free BTMC molecule in $CHCl_3$ (green trace) and the host–guest complex (red trace) in the wavelength range of 240 nm to 600 nm. The empty cage in water shows an absorption maximum at 256 nm, tailing to 380 nm. Free BTMC in $CHCl_3$ has an absorption maximum at 370 nm while it extends up to 420 nm (as shown in Fig. S5). The host–guest complex of BTMC⊂Cage having a distinct yellow color has absorption features of both the free cavity (maximum at 256 nm) and individual molecule absorption at 370 nm along with an extended band which now goes up to 450 nm (as shown in the inset of Fig. 2c). The broadening of the absorption spectrum indicates the formation of a host–guest complex which leads to the intense yellow color of the solution. Previous work has shown that such extended absorption features can have charge transfer character,[19,24,26] although in this case, the local excitations of the molecule could also be broadened due to cage incarceration and heterogeneity of packing. However, it is unequivocal that the host–guest complex between an electron rich bithiophene molecule and the electron deficient cage is stable, and can be photoexcited for carrying out C–H bond oxidation reaction as shown previously for toluene incarcerated in the cage.[26]

### Selective photoproduct upon visible light excitation

In order to test the C–H bond photoactivation reaction, we irradiated the aqueous solution containing 12.5 mM BTMC with 20 mol% cage using a 400 nm LED light (50 mW) source for 24 h. We observed a color change at the end of reaction while the photoproducts were extracted in $CHCl_3$ and analyzed by GCMS and $^1$H NMR spectroscopy. Fig. 2d shows the product distribution with the GC retention time. We observe only one product with a mass of 222 Da which was identified as the oxidized product, 2,2′bithiophene-5,5-carbaldehyde and also confirmed by $^1$H NMR spectra (Fig. S6 and S7). The formation of a single selective photoproduct *via* oxidative functionalization of the $-CH_3$ group to –CHO is analogous to the toluene oxidation to benzaldehyde.[26] It should be noted that such selective transformations in substrates with a thiophene backbone have been challenging.[43–45] The mechanism to explain this oxidized product formation should therefore involve formation of a neutral radical on the $-CH_3$ group triggered by PCET driven C–H activation followed by reaction with dioxygen gas under ambient conditions.[26,46] To confirm the role of oxygen in the

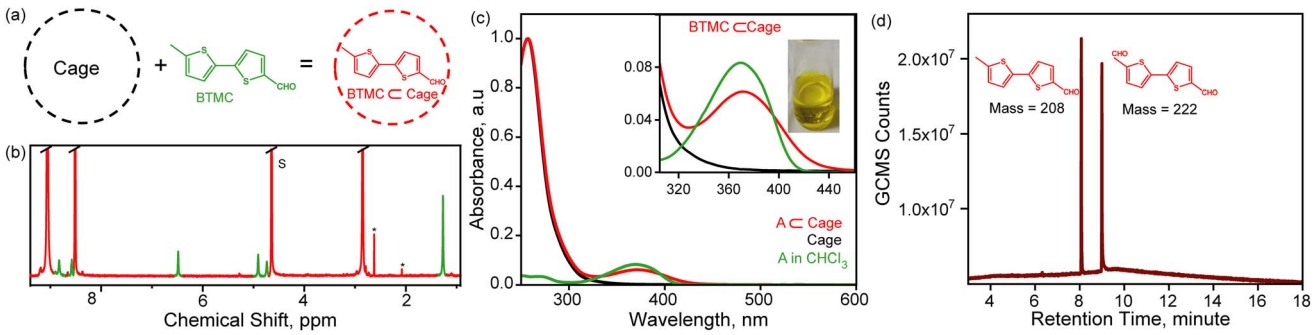


Fig. 2 Characterization of host–guest complex and photo-redox reaction. (a) Concept of incarceration of BTMC inside the water soluble cage. (b) NMR characterization of host–guest complexation. The green colored peaks denote the molecule NMR inside cavity. (c) Absorption of BTMC⊂Cage is shown (red trace) in comparison to free cage (black trace) and BTMC in $CHCl_3$ (green trace). (d) GCMS trace showing product formation after photoreaction of BTMC⊂Cage.

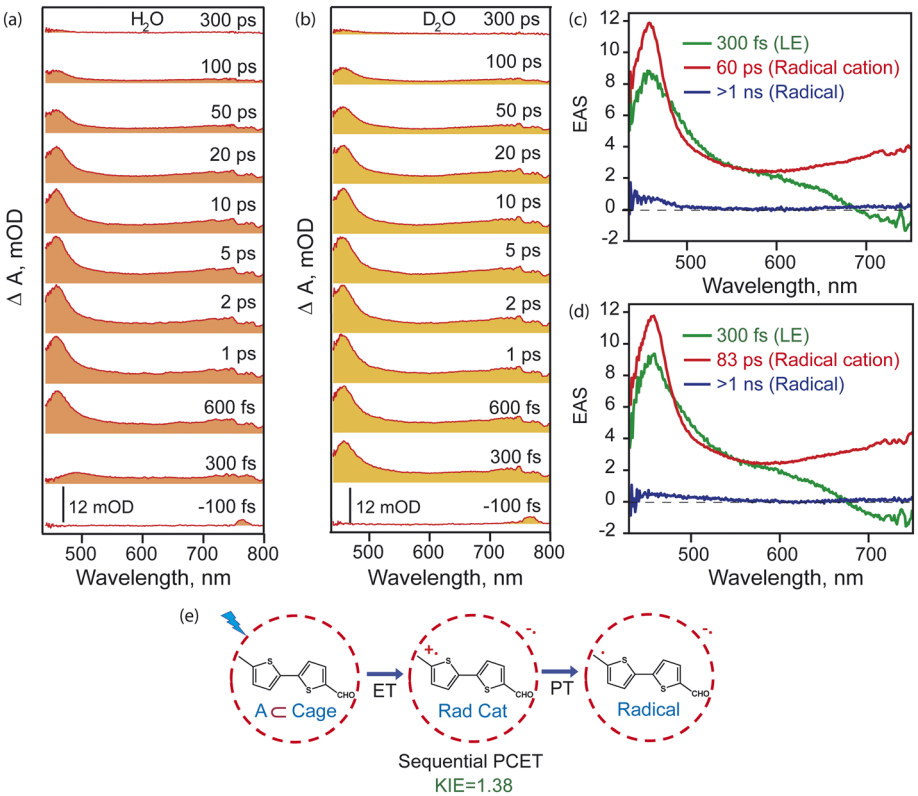


Fig. 3 Transient absorption spectra and dynamics. Femtosecond-to-nanosecond transient absorption of BTMC⊂Cage in the probe region of 430–800 nm on 400 nm excitation in (a) $H_2O$ and (b) $D_2O$. SVD of the entire spectra using a three state sequential model showing the evolution associated spectra in (c) $H_2O$ and (d) $D_2O$. (e) Reaction mechanism of sequential PCET of BTMC⊂Cage as observed from fs-ns TA.

photoreaction, we performed the reaction under both ambient and inert (under argon atmosphere) conditions. We found negligible product formation under inert conditions showing the role of oxygen in photo-oxidation as characterized by GCMS and $^1$H NMR spectroscopy (SI Fig. S6 and S7). We also monitored the photoreaction in $D_2O$ without extracting the unreacted substrate and aldehyde photoproduct. The $^1$H-NMR spectrum shows a decrease in BTMC guest proton peaks, and the appearance of new proton peaks corresponding to the product as shown in Fig. S8 and S9. To confirm the photoinduced sequential PCET mechanism in the case of the BTMC⊂Cage complex, we next performed transient absorption spectroscopy and FSRS.

### Excited state dynamics of BTMC⊂Cage

To track the dynamics of potential radical intermediates at the –$CH_3$ site in BTMC after host–guest photoinduced charge transfer, transient absorption (TA) spectroscopy was carried out. Femtosecond transient absorption traces of BTMC⊂Cage subsequent to photoexcitation at 400 nm were recorded in both $H_2O$ and $D_2O$. Fig. 3a shows the TA traces in the probing window between 430 nm to 800 nm from negative 100 fs to 300 ps in $H_2O$. We observed a rise in the excited state absorption feature (ESA) having maxima at 458 nm until ~1 ps. Along with the sharp absorption feature, there is also a broad absorption feature throughout the visible region with lower oscillator strength up to 750 nm. Our TA feature matched the known bithiophene radical cation spectra from previous flash photolysis experiments.[47] We, however, observed a slightly red-shifted spectrum due to the additional[48] chemical appendages on the molecule such as the –$CH_3$ and –CHO moieties as well as it being incarcerated inside a cationic cavity with host–guest interactions. Such red-shifts have been previously observed for radical cation spectra associated with poly-aromatic hydrocarbons inside the cage.[26] Thus, the TA features could be assigned to the formation and decay of BTMC radical cation inside the cavity. The entire ESA decays by 100 ps where there is a change in the absorption feature, and by 300 ps we see that there's a very low oscillator strength absorption remaining on the blue side of the probe region from 440 nm to 500 nm.

In order to test a possible protonation/deprotonation step after the radical cation formation, we also measured the TA traces for BTMC⊂Cage in $D_2O$ (Fig. 3b). We find that exactly similar features were obtained although with slightly modified kinetics. The inherent dynamics of states were deconvoluted from the entire TA spectral dataset using a three-state sequential model and singular value decomposition (SVD) to obtain the lifetime and absorption spectra of each species (details in the SI). Fig. 3c and d shows the evolution associated spectra (EAS) of all the components and their respective lifetimes in both $H_2O$ and $D_2O$. The green spectral trace represents the host–guest complex local excited (LE) state whose lifetime is ~300 fs. Although one would expect that the 400 nm photo-excitation leads to $S_1$ of the BTMC molecule, the electronic structure of the

incarcerated BTMC molecule could already have mixed-in charge transfer character. Therefore, in all subsequent discussions in the manuscript, we assign the LE to have CT character inside the cage, and its evolution to the radical cation state arises only after a formal electron transfer (ET) to the cage. This ET timescale of ~300 fs is independent of solvent isotope effect. The red trace shows the radical cation absorption of BTMC⊂Cage with a lifetime of ~60 ps in $H_2O$. Interestingly, the spectrum of the radical cation state bears close similarity to the spectrum assigned to the LE state which indicates that the initial excited state has strong hybridization of the BTMC and cage molecular orbitals due to charge transfer character. The decay of this radical cation is expected to occur *via* deprotonation of the $-CH_3$ group of the BTMC molecule, thereby giving rise to the neutral C-site radical. This deprotonation happens due to the presence of a pre-organized solvent shell of water molecules which acts as a proton acceptor. Hence, a secondary KIE is expected when we change the solvent from $H_2O$ to $D_2O$ with dependence on the BTMC radical cation lifetime.

Although the initial electron transfer timescale of 300 fs remains the same in $D_2O$ (green trace in Fig. 3d), the radical cation (red trace in Fig. 3d) lifetime is now elongated to ~83 ps showing a secondary KIE of 1.38. Such a KIE is expected for the sequential PCET reaction.[49] Single point kinetics clearly showing slower decay of the radical cation state at 460 nm in $D_2O$ *vs.* $H_2O$ is shown in Fig. S10. Thus, indeed there is a deprotonation step involved as seen from the $H_2O$ *vs.* $D_2O$ dependence of the dynamics of the BTMC radical cation in the cavity. In both $H_2O$ and $D_2O$ there is a long-lived component (blue trace in Fig. 3c and d) with low oscillator strength which is presumably the BTMC neutral radical spectrum inside the cage cavity. The global analysis along with single point kinetics showing the quality of data fitting is presented in Fig. S11 and S12.

We also probed the NIR region to observe the extent of the radical cation spectrum and to monitor the host–guest CT state dynamics. The transient absorption in the NIR region is shown in Fig. S13. Evolution in the absorption spectra is shown from negative 100 fs to 300 ps in $H_2O$. We find a blue shift of the entire spectra with time. This feature in the NIR region has been assigned to a coupled host–guest radical cation and radical anion state based on previous work.[24] The blue shift of the transient spectrum describes the solvent reorganization in the host–guest charge transfer excited state. Single point kinetics at 880 nm of the TA data (Fig. S13b and c) show a rise time of 1.55 ps which is the solvent reorganization timescale in $H_2O$ and 1.77 ps in $D_2O$. A similar KIE is seen in the decay of the radical cation state showing deprotonation. Thus, from our TA measurements, we conclude that upon excitation of the host–guest complex at 400 nm there is an electron transfer representing host–guest charge transfer with a ~300 fs timescale which gives rise to the radical cation state which then undergoes deprotonation showing a secondary KIE of 1.38 to give a neutral radical state. Fig. 3e shows the probable pathway for radical formation through steps of electron transfer and proton transfer as also previously observed in such host–guest systems. Thus, an ET followed by a PT which shows a significant secondary kinetic isotope effect (KIE) marks a sequential PCET mechanism.

In order to ascertain that the excited state dynamics indeed arise due to a charge transfer process from the confined BTMC molecule, the excited state dynamics of free BTMC in $CHCl_3$ were studied after photoexcitation. From the steady-state absorption and emission spectra of BTMC in $CHCl_3$ (Fig. S5), we see strong emission of the free molecule with an emission maximum at 436 nm. The fluorescence lifetime as measured by TCSPC with an IRF of ~60 ps (Fig. S14) shows a decay of 1.39 ns for an emissive state that rises with a ~57 ps time-constant. The data indicate that the local $S_1$ state in BTMC is long lived till 1.39 ns with an internal conversion timescale of 57 ps within singlet states. Broadband transient absorption measurement of BTMC in $CHCl_3$ (Fig. S15) shows a rise time of ~24 ps in the ESA which subsequently leads to a biexponential decay with time constants of 1.2 ns (53%) and >2 ns (47%) (single point kinetics in Fig. S16). The ~24 ps timescale corresponds the same process that was measured by TCSPC with much poorer time resolution. It is well known for bithiophene frameworks that intramolecular charge transfer states[33,50] can form in tens of picoseconds and can be polarity sensitive. Therefore, the rise time of ~24 ps apparently corresponds to evolution to an emissive singlet state which is attributed to planarization of the bithiophene backbone as well as solvent reorganization on the excited state. The longer timescale dynamics were probed using nanosecond-microsecond transient absorption spectroscopy. Fig. S17 shows the spectra collected between 1 nanosecond and 300 nanoseconds, which are assigned to the long-lived triplet state. Single point kinetics at 480 nm show a biexponential decay, first of a singlet state with a lifetime of 1.35 ns while a triplet state is observed with a 224 ns lifetime (Fig. S18). The formation of BTMC triplets in $CHCl_3$ contrasts with the dynamics of the sequential PCET pathway of the BTMC⊂Cage solution which ultimately leads to C–H bond photoactivation.

### FSRS dynamics during C–H bond activation

To watch the structural changes as the $sp^3$ $-CH_3$ site evolves to an $sp^2$ $-CH_2$ radical, we carried out FSRS to capture the Raman snapshots of the photoinduced sequential PCET chemistry. We assigned all the ground state Raman features of the host–guest complex using spontaneous CW Raman measurements. Raman spectra of the free cage and BTMC⊂Cage were recorded under CW laser irradiation at 488 nm to assign the cage modes,[19] and the BTMC molecular modes inside the cavity-confinement in the ground state (Fig. S19). We separately collected the stimulated Raman spectrum with an 814 nm Raman pump (additional information about the stimulated Raman experiment is provided in the SI) for both 5 mM BTMC in DCM (Fig. 4a; black trace) and 5 mM cage in $H_2O$ (Fig. 4b; blue trace) in the ground state (all analysis procedures are described in the SI). In order to assign the normal modes in the ground state, electronic structure optimization along with normal mode analysis of BTMC was performed using DFT at the CAM-B3LYP/6-31g(d) level while the cage modes were already established from previous work.[19] Fig. 4a shows the ground state stimulated Raman

spectrum of BTMC and its normal mode description (Fig. S20) with the most intense Raman modes. As shown in Fig. 4b, the ground state stimulated Raman spectrum of the BTMC⊂Cage complex was then fitted to Gaussian peak functions to get a fitted spectrum (red line in Fig. 4b). The 1475 $cm^{-1}$ mode arises from the symmetric C=C stretching of the thiophene rings while both the 1425 $cm^{-1}$ and 1557 $cm^{-1}$ modes arise from asymmetric C=C stretching of the thiophene rings (Fig. 4a and S20). The 1668 $cm^{-1}$ mode is assigned to the C=O stretching of the aldehyde group. Many of the BTMC modes inside the cavity were prominently observed with 1472 $cm^{-1}$ being the most intense Raman active mode (Fig. 4b). This mode however was 3 $cm^{-1}$ red-shifted potentially due to interactions with the cationic nanocage. In addition, the asymmetric C=C stretch was 2 $cm^{-1}$ red-shifted while the 1655 $cm^{-1}$ mode assigned to the C=O stretch was 13 $cm^{-1}$ red-shifted from the observed frequency in DCM. The large red-shift in the C=O stretch arises from the hydrogen bonding interactions[19] of the aldehyde group with surrounding water molecules that may be at the interface of the pores in the cavity.

To understand the excited state structural changes associated with the steps of radical cation formation and its evolution to a neutral radical state through sequential PCET, time-resolved stimulated Raman spectra (see details in the SI) were recorded subsequent to 400 nm femtosecond pump pulse excitation. The Raman excitation pulse was kept at 814 nm which was in pre-resonance with the excited state absorption of the radical cation feature at ~750 nm extending into the NIR region. This ensures that the resonance Raman features of the radical cation state will dominate over all other modes including the cage features. Fig. 4c shows the evolution of the excited state FSRS spectra at various time delays. The excited state Raman features were extracted after few steps of data handling which involved ground state removal by 1 : 1 subtraction and baseline correction as elaborated in the SI. We observe that the excited Raman peaks take time to build up after the formal $t = 0$ after photoexcitation. The initial time traces from 200 fs to 3 ps in Fig. 4c show spectral features in three distinct regions: (a) features at 1514 $cm^{-1}$ and 1432 $cm^{-1}$, (b) a feature at ~1215 $cm^{-1}$ and (c) a broad feature at ~990 $cm^{-1}$. It is well known that the high frequency modes around 1400–1600 $cm^{-1}$ arise from the C=C stretching frequencies of the bithiophene ring radical cation state as reported in the literature.[48] The sub-picosecond rise time of these features indicates that stimulated Raman spectral features of the neutral excited state (LE) are potentially buried under the resonance-enhanced radical cation Raman spectra although we did carry out singular value decomposition to extract the LE features. The lower frequency modes at 989 $cm^{-1}$ and 1222 $cm^{-1}$ are assigned to C–H bending modes coupled to the C=C stretches. At later time points from 10 ps to 75 ps, we observe intensity decay of the high frequency modes while new lower frequency modes seem to appear at 1040 and 1181 $cm^{-1}$. The observed changes in the relative spectral intensities and frequencies of the modes clearly indicate structural evolution of the bithiophene backbone during the C–H bond activation chemistry.

In order to analyze the dynamics of the modes, we carried out kinetic fits for the major peaks as well as global fits to the

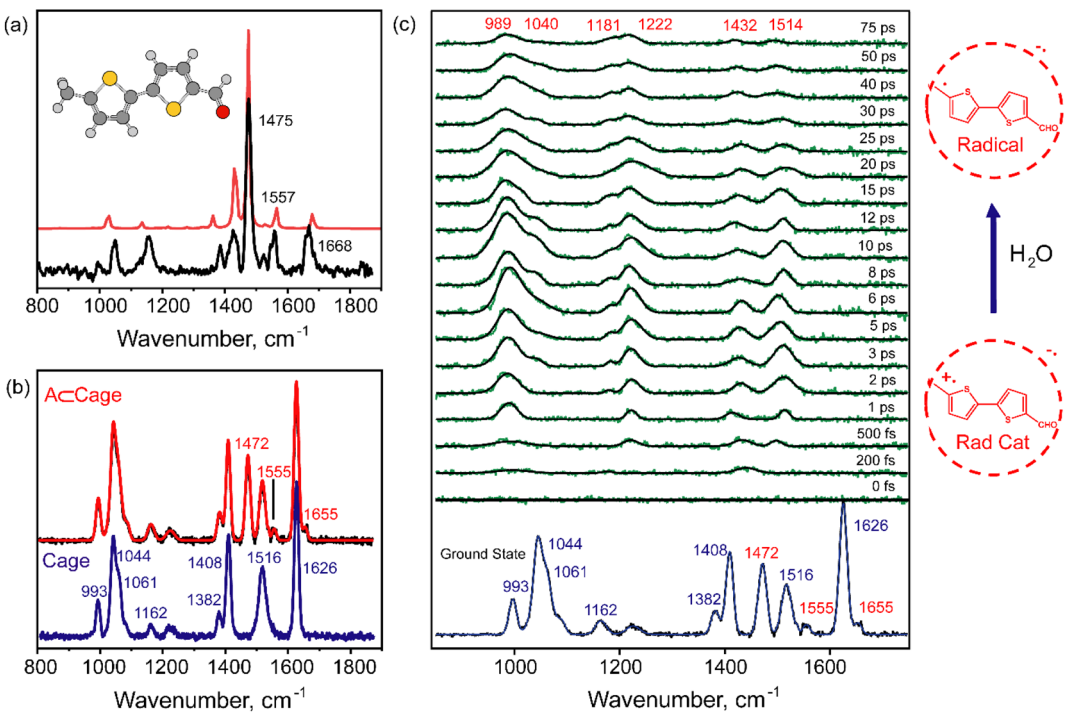


Fig. 4 Transient Raman snapshots of C–H bond breaking. (a) The ground state stimulated Raman spectrum of the free BTMC in dichloromethane (DCM) is compared to the computational Raman spectrum. The principal modes are all marked. (b) Ground state stimulated Raman spectra of only cage and BTMC incarcerated inside the cage; the latter shows both the Raman features of the guest and the cage. (c) Resonance selective transient stimulated Raman spectra of the BTMC radical cation as it undergoes sequential proton-coupled electron transfer.

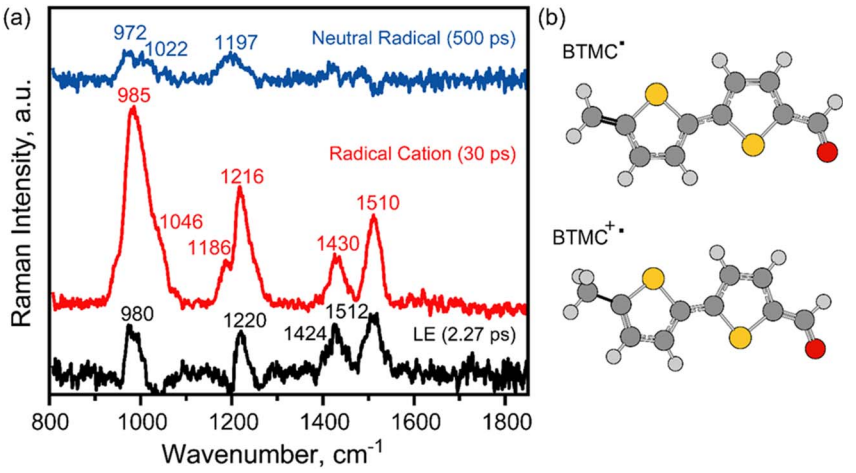


Fig. 5 (a) SVD of FSRS data showing distinct features of the LE, radical cation and neutral radical modes. The spectral traces have been offset for clarity. (b) Structural change of BTMC from the radical cation to the neutral radical state through PCET.

entire FSRS data. The most intense Raman modes at 1432 and 1514 $cm^{-1}$ in Fig. 4c potentially mark the rise and decay of the radical cation state. Fig. S21 shows the decay of the integrated areas of the peaks at 1432 and 1514 $cm^{-1}$ respectively. A rise time of ~0.6 ps and a mono-exponential decay of 30 ± 10 ps were observed for the integrated peak area of the 1514 $cm^{-1}$ mode. It should be noted here that the large errors in the fits reflect the peak area scatter in the obtained experimental data. The 1432 $cm^{-1}$ mode however showed a rise-time of 2 ps with a decay of 40 ± 10 ps. Thus, the dynamics of our FSRS data show a dispersion of timescales for both the modes while indicating perhaps a faster 30–40 ps decay of radical cation as compared to the ~60 ps decay observed from our TA experiments.

To increase the robustness of the timescales associated with radical cation decay from FSRS experiments compared to TA, we globally analyzed the FSRS data using a 3-state sequential model analogous to the TA dataset. We found that we can globally fit the data with 3 individual components, and extract stimulated Raman spectra of the host–guest complex LE state, the radical cation state and the neutral radical state. We find that a LE state lifetime of 2–3 ps fits the data well while being similar to the TA data. Our fits for the radical cation show that when radical cation lifetimes are varied between 14 and 30 ps, the obtained deconvoluted stimulated Raman spectra of all the three states are robust. The stimulated Raman spectra of the LE, radical cation and neutral radical states are plotted in Fig. 5. Both single-point kinetics and kinetics from SVD are shown in SI Fig. S21 and S22. If we constrain the radical cation lifetime beyond 30 ps, we immediately observe that the fits are not good enough and the deconvolved Raman spectra exhibit baseline artifacts since the FSRS dataset beyond 75 ps has a low S/N ratio. The deconvoluted radical cation Raman spectrum is characterized by intense modes at 985 $cm^{-1}$, 1216 $cm^{-1}$, 1430 $cm^{-1}$ and 1510 $cm^{-1}$. This spectrum has modes that compare well with the experimental resonance Raman data of the bithiophene radical cation spectrum obtained by Jensen *et al.* using nanosecond time-resolved Raman spectroscopy with 425 nm excitation at low temperature.[47] Peaks at 1535, 1435, 1358, 1276, 1219, 1166, 1070 and 979 $cm^{-1}$ respectively characterize the experimental radical cation Raman spectrum from previous work. Our peaks at 1510, 1430, 1216, 1186, 1046 and 985 $cm^{-1}$ make the FSRS-obtained spectra a reasonable match although our spectral resolution is ~16 $cm^{-1}$ while the peak widths are ~30–40 $cm^{-1}$. It should be noted that CT interactions with the cage as well as interactions with water can potentially shift the mode frequencies in the radical cation state although most of the modes have similar peak positions. The extracted neutral radical Raman spectrum resembles the spectra in the raw FSRS data that remain after 30 ps characterized by two main features at 972 $cm^{-1}$ with a 1022 $cm^{-1}$ shoulder and at 1197 $cm^{-1}$ as the major modes with low intensity transitions at 1420 $cm^{-1}$ and 1480 $cm^{-1}$ respectively. It is reasonably clear that the removal of the proton from the $-CH_3$ group would extend the conjugation of the thiophene rings to the $-CH_2$ group, thereby enhancing the relative intensity of the C–H in-plane bending modes in the ~900–1100 $cm^{-1}$ region.

Interestingly, we could also deduce an LE state Raman spectrum which seems to have features very similar to those of the radical cation Raman spectrum although with a lower signal-to-noise ratio. Thematically, it matches well with our TA data which also show spectral similarity of the initial LE state which already has a charge transfer or partial radical cation character. In fact, both FSRS and TA suggest that CT interactions of BTMC with the cage sufficiently modify the excited states accessed with a 400 nm pump pulse so that we observe the precursor CT state before the radical cation formation. Since resonance FSRS dominates along with the larger Raman cross section of a potentially planar radical cation framework, the radical cation spectrum is more sensitively detected and dominates any observable LE state of the host–guest complex with neutral BTMC. In summary, using global analysis, we robustly elucidate the Raman spectrum of the proton-abstracted neutral radical which is very distinct from the radical cation state marking the loss of the proton from the $-CH_3$ group. It also uncovered that the proton transfer (PT) timescales can be heterogeneous on the tens of picoseconds as determined

by the combination of femtosecond stimulated Raman and transient absorption spectroscopy.

In an attempt to assign the excited state modes, electronic structure optimization with normal mode analysis was performed for BTMC in the gas phase since vibrational calculations for host–guest CT states are computationally challenging. For comparison, we still computed the Raman spectrum of the locally excited $S_1$ state for BTMC molecules, an artificially created BTMC radical cation in its $D_0$ and $D_1$ states, and the corresponding neutral radical in its $D_0$ and $D_1$ states. We compared our FSRS data to the computed Raman spectra for the $D_0$ state since it is energetically accessible from the LE state of the BTMC molecule. The changes in bond lengths and dihedral angles for all the optimized geometries are given in Fig. S23. The computed Raman spectra for $S_1$ of BTMC, $D_0/D_1$ of the radical cation BTMC and $D_0/D_1$ of the BTMC radical are compared while the comparison with the ground state is shown in Fig. S24. As expected, the extracted FSRS spectrum of the LE state does not match the computational vibrational spectra in the $S_1$ state of the isolated neutral BTMC molecule. This is observed because upon incarceration of BTMC in the cage and excitation with light a charge transfer state is formed. In fact, the $S_1$ Raman spectrum should have shown just one intense C=C stretching peak at 1524 $cm^{-1}$ while the rest of the modes have low polarizability.

The computed Raman spectrum of the gas-phase radical cation $D_0$ state shows an intense mode at 1505 $cm^{-1}$ for C=C stretching (Fig. S24b) along with a mode at 1710 $cm^{-1}$ for the carbonyl group. Along with these modes, we also find lower polarizability for the Raman lines associated with C=C stretching at 1380 $cm^{-1}$, 1404 $cm^{-1}$ and 1460 $cm^{-1}$ on two unsymmetric thiophene rings. The mode at 1160 $cm^{-1}$ corresponds to the C–H in plane bending mode coupled to C=C stretching of the backbone while weak bands are seen in the 1060 $cm^{-1}$ region also. A direct comparison of the SVD extracted Raman data suggests that some experimental FSRS peaks could be explained by the computed gas-phase $D_0$ state although most of the modes are supported by the experimental data obtained by Jensen *et al.*[47] Therefore we believe that a more accurate calculation with BTMC incarcerated inside the cage having an anion radical is required to completely simulate the experimental BTMC radical cation FSRS spectrum.

For the neutral radical $D_0$ state computations, we see enhanced Raman intensities at 1017 $cm^{-1}$, 1175 $cm^{-1}$, 1280 $cm^{-1}$ and 1367 $cm^{-1}$ respectively (Fig. S24c). Additionally, less intense peaks at 1428 $cm^{-1}$ and at 1480 $cm^{-1}$ are also observed. The normal modes with displacement vectors of the most intense Raman modes in the BTMC neutral radical $D_0$ state are shown in Fig. S25. We find that our FSRS data do not completely align with the predicted $D_0$ state of the free BTMC neutral radical. Interestingly, we cannot rule out the energetic accessibility of the $D_1$ state from the $D_0$ state for the cage-confined BTMC neutral radical. We hypothesize that due to strong interactions with the cage anion radical as well as specific water interactions with the BTMC backbone, the $D_1$ state can be stabilized under confinement. We therefore find it reasonable to compare the computed $D_1$ Raman spectrum with our obtained neutral radical FSRS spectrum at long time delays especially from 30–60 ps. We find that the major peaks at 996 $cm^{-1}$ and 1155 $cm^{-1}$ in the computations (normal modes shown in Fig. S25) match favorably with our features at 972 $cm^{-1}$ and 1197 $cm^{-1}$ while smaller features at 1390 $cm^{-1}$ and 1450 $cm^{-1}$ are also observed similar to our SVD extracted features at 1420 $cm^{-1}$ and 1480 $cm^{-1}$ respectively. We find that our experimental FSRS spectra of the neutral radical indeed match better with the computed $D_1$ state although we cannot track its decay to the final $D_0$ state in the FSRS experiment. The geometry change results in planarization of the bithiophene framework either in its $D_1$ or $D_0$ state although further high-level calculations are required in future to compute the Raman spectrum of the BTMC radical states when incarcerated inside the cage in its anion radical state. We therefore conclude that deprotonation at the $–CH_3$ site and formation of a $–CH_2$ radical, as visualized by FSRS, introduce double bond character to the $C_9–C_{10}$ bond, which, now in conjugation with the bithiophene backbone, enhances the Raman intensities of the adjacent C–H bending modes. The decay of the high frequency C=C stretching modes and the rise of C–H bending modes mark the formation of the neutral radical or the activated carbon-site.

Fig. 5 shows the structural change along this excited state pathway along with the evolution in the Raman spectra from BTMC in the LE state to the radical cation and subsequently to the neutral radical state. The optimized nuclear geometry of the ground state and first excited state of the radical cation and neutral radical are shown in Table S1–6. We observe that the thiophene rings in the ground state for BTMC are out of plane with a $S_2–C_6–C_5–S_1$ dihedral of 169.72°. Typically for the free BTMC molecule, in the first excited state there is partial attainment of planarity and a subsequent increase in π-conjugation in the bithiophene backbone as seen from the BTMC $S_1$ bond lengths and dihedral angles. However in our case $S_1$ is not observed due to increased CT character once the BTMC is confined inside the cage which is an electron acceptor. In the radical cation state, which is a one-electron removed species from BTMC there is even higher π-delocalization and planarity in the ground $D_0$ state or even in the $D_1$ state. Upon analyzing the neutral radical structure as compared to the radical cation the deprotonation at the $–CH_3$ group forms a $–CH_2$ $sp^2$ site which can now have a partial double bond character due to conjugation with the bithiophene rings. This is depicted in the shortening of $C_9–C_{10}$ bond lengths in Fig. S23 for the neutral radical state.

An alternate viewpoint can be proposed that involves Raman detection of cage anion radical modes mixed with the evolution of the BTMC radical cation to the BTMC neutral radical features. However, careful analysis of the cage anion radical modes (shown in Fig. S26) with respect to the neutral cage modes shows multiple tripyridyltriazine (TPT)-centric ligand modes are expected between 1300 to 1700 $cm^{-1}$ with reasonable intensity including a few beyond 1500 $cm^{-1}$ which are not observed in our FSRS spectral evolution. Additionally, these TPT-centric modes should have a clear distinction in temporal decay dynamics compared to the BTMC radical cation modes which decay within 14–30 ps. As the cage anion radical should

be observed throughout the BTMC evolution dynamics, we do not observe any such temporally distinct TPT-centric modes which could signify any detectable cage anion radical modes. Taken together with the resonance enhanced Raman signals of the BTMC radical cation and neutral radical features, we rule out any possibility of cage anion contributions to the FSRS evolution in tens of picoseconds.

### FSRS dynamics and reaction coordinate

In summary, the FSRS data along with all assignments clearly indicate that the radical cation state can be discriminated using the Raman spectrum unlike the transient absorption data, where the states appear similar with broad features although with distinct oscillator strengths. Additionally, the proton transfer timescales scored by FSRS lie broadly between 14 and 30 ps, much faster than ~60 ps TA rates. To us, this suggests that in transient absorption the spectral changes accommodate both the deprotonation dynamics of formal C–H bond-breaking along with other associated structural relaxation, *e.g.* the equilibration of the incipient proton with the interacting water cluster. The difference in apparent timescales between FSRS and TAS arises fundamentally from the different observables probed by the two techniques. FSRS directly tracks the evolution of vibrational coherences and frequencies, which are sensitive to structural relaxation on the excited-state potential energy surface, and can be insensitive to changes in electronic oscillator strength. In contrast, TAS signals explicitly depend on the electronic transition strengths and the populations. Thus, changes in oscillator strength during relaxation can significantly alter TAS amplitudes and kinetics without reflecting changes in the underlying structural dynamics. Our results thus indicate that there can be heterogeneity in deprotonation rates in this host–guest CT system, and solely transient absorption signatures for interpreting proton transfer timescales may be insufficient. Therefore, it is best to complement the TA measurements with time-resolved vibrational spectroscopy to disentangle the timescales of definite structural changes from the electronic state changes.

FSRS provides vibrational signatures of the structural change that occurs during the formation of the neutral radical which has increased backbone conjugation compared to the radical cation state. The $C_9$–$C_{10}$ bond attains partial double bond character and hence the tetrahedral carbon becomes planar after deprotonation. This is marked by the rise in intensity of the C–H bending modes adjacent to the methyl group. Interestingly the ~60 ps deprotonation dynamics from transient absorption spectroscopy has a KIE of ~1.4 when $D_2O$ replaces the solvent water. As FSRS indicates a 14–30 ps proton dissociation timescale, we reinterpret the transient absorption dynamics to include not only the fundamental deprotonation step but also proton hopping within the associated water cluster in stabilizing the neutral radical state. Traditionally, the KIE in PCET provides information about the distances associated with the donor and acceptor, with small KIEs of ~1.1 representing short proton hopping distances. In future, we plan to mechanistically understand how extensive hopping within the water cluster increases the value to ~1.4 using detailed molecular dynamics simulations which include solvation of the host–guest complexes. We, therefore, conclude that water cluster rearrangements around the BTMC $C_{10}$–H bond should be a crucial reaction-coordinate enabling proton stabilization as a base after C–H bond cleavage from the radical cation. Our measurements fall in line with the work of Hammes-Schiffer and co-workers who predicted that excited state sequential PCET reactions should also have a dominating solvent rearrangement coordinate. We believe that in future in-depth multidimensional 2D electronic-vibrational spectroscopy along with impulsive excitation might unravel all the low-frequency modes associated with formation of the radical cation state and ensuing deprotonation on the excited state. Additionally, as mentioned previously the FSRS mode frequencies of the radical cation and neutral radical states cannot be directly compared to gas phase calculations of free BTMC molecules, and detailed computations considering all atoms explicitly are required for the host–guest CT systems in future. Once these frequencies are computed, *ab initio* molecular dynamics simulations could also reveal the rich water dynamics during the sequential PCET step that enables cage-confined photoredox catalysis.

Recently, Fleming and co-workers showed excited state PCET occurring *via* two reactive pathways of fast PCET (minor pathway, 4%) and a relaxed PCET (major pathway, 96%) in a bio-mimetic benzimidazole–phenolpentafluoro phenylporphyrin (BIPPF15) complex through two-dimensional electronic-vibrational spectroscopy.[51] Their work illustrates that in cases where the proton acceptor and electron acceptors are in the same framework heterogenous pathways for PCET may exist making it difficult to use a single-reaction coordinate description. In contrast, we find that if a pre-organized water cluster interacts with the guest inside the cavity, one can have a single PCET pathway with separate electron and proton acceptors. Our work also contrasts with the concerted PCET pathways in excited state described by Mayer and co-workers in the inverted Marcus region.[52] We thereby have generated an optimized situation for a non-equilibrium PCET reaction inside a cavity that can be exploited for high efficiency C–H bond functionalization reactions in water.[25] The significance of the pre-organized water cluster therefore is to provide functional water molecules that act as a co-factor to the actual cationic nanocage catalyst for removing charge buildup by providing a proton-transfer network on the ~10–100 picosecond timescale. Our photoredox strategy here complements the classical diffusion-based paradigm initially popularized by Macmillan and co-workers and now used extensively.[53]

## Conclusions

To summarize, we track the primary steps of ultrafast C–H bond photoactivation within a water-soluble supramolecular cavity using a synergistic combination of transient absorption and femtosecond stimulated Raman spectroscopy (FSRS). As shown in Fig. 6, we demonstrate selective aldehyde formation at a terminal –$CH_3$ group appended to a bithiophene backbone *via* a well-defined photoinduced proton-coupled electron transfer

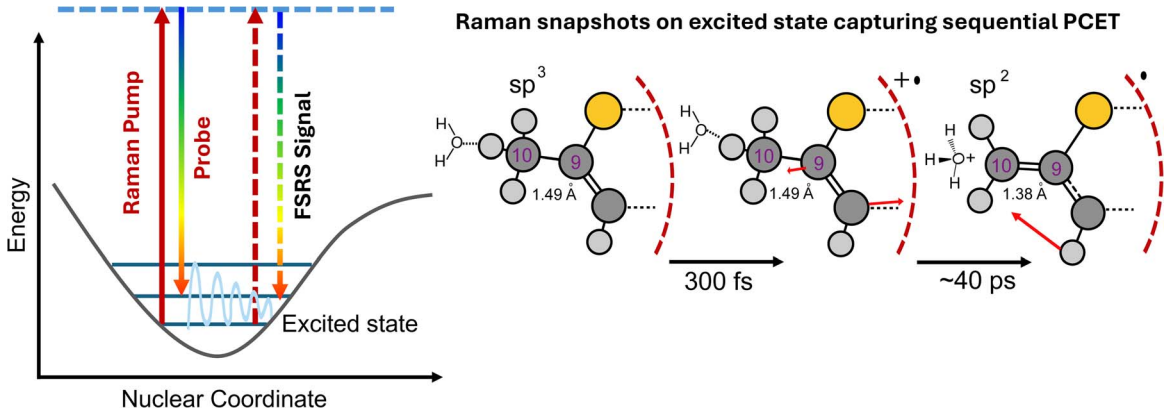


Fig. 6 PCET dissected with excited state stimulated Raman. FSRS measurements reveal the structural dynamics of the C–H bond activation reaction. It proceeds through a radical cation intermediate whose structure evolves into the planar neutral radical confined inside a water-soluble nanocage.

(PCET) mechanism along a host–guest charge transfer (CT) potential energy surface. Rich vibrational dynamics—particularly thiophene C–H in-plane bending modes coupled with C=C stretches—provide unequivocal evidence of the C–H bond breaking step, as the radical cation state is resonantly enhanced in our FSRS data. The emergence of shifted vibrational modes following deprotonation marks the formation of the neutral radical within ~14–30 ps which is certainly faster than changes observed by probing the excited state absorption features *via* transient absorption spectroscopy which are sensitive to population decay, relaxation and oscillator strength changes. A pronounced secondary kinetic isotope effect in $D_2O$, along with insights from the vibrational "Raman movie" highlights the critical role of a closely interacting water cluster in facilitating deprotonation while potentially highlighting heterogeneity in the proton transfer step. Our work therefore provides the first structural visualization of an ultrafast PCET-triggered C–H activation event, revealing how substrate interaction with water clusters stabilizes on-pathway intermediates in real time. We envision that the synthetic community would use modular host–guest strategy for harnessing photoinduced PCET reactions in aqueous environments for targeted organic transformations.

## Author contributions

J. D. conceived the research, and planned the initial experiments with A. D. and S. P. The original synthesis, characterization, time-resolved spectroscopy and FSRS measurements were carried out by S. P. while the data were analyzed by S. P. with help from J. D. A. D. carried out the initial work of characterizing host–guest complexes of bithiophene substrates for the FSRS measurements. Shashi carried out additional characterization of the host–guest complexes and provided control experiments on photoreactivity of the host-guest complexes. The electronic structure calculations along with Raman calculations for BTMC were performed by S. P. while few model calculations were done by Shashi. Computations for extracting the Raman spectrum of the neutral cage and its anion radical was performed by D. M. The manuscript was written by S. P., Shashi, A. D. and J. D. with contributions from D. M. All the co-authors discussed the scientific content in detail and approved the final version of the manuscript.

## Conflicts of interest

There are no conflicts to declare.

## Data availability

The data supporting this article have been included as part of the supplementary information (SI). Supplementary information: description of the materials and experimental methods, additional figures pertaining to the experiments. See DOI: https://doi.org/10.1039/d5sc05247e.

## Acknowledgements

S. P., Shashi, A. D. and J. D. acknowledge support from the Department of Atomic Energy (DAE), Government of India, under Project no. 12-R&D-TFR-5.10-0100. D. M. acknowledges funding from the Ramon y Cajal grant RYC2020-029863-I through the Instituto de Ciencia de Materiales de Madrid, Consejo Superior de Investigaciones Cientificas (CSIC-ICMM), PIE grant from CSIC-ICMM (20226AT001), and the Spanish Ministerio de Ciencia, Innovacion y Universidades grants (PID2019-111086RA-I00, TED2021-1327 57B-I00, PID2022-143013OB-I00, and CNS2023-145046). The authors would like to specially thank Prof. Sharon Hammes-Schiffer (Princeton University), Prof. Ayan Datta (IACS Kolkata) and Chandralekha (IACS Kolkata) for helpful discussions and collaborative ideas. We also thank Prof. Vamsee Voora (TIFR Mumbai) for discussion on electronic structure calculations. The authors acknowledge the discussions with Dr. Arup Kundu, Dr. Dipin Tomer, Dr. Debojyoti Roy, and Dr. Kishan Yadav (TIFR Mumbai). The authors thank Mrs. Mamta Kallianpur (TIFR Mumbai) for help in the TCSPC measurements.

## References

1 A. H. Zewail, Laser selective chemistry—is it possible?, *Phys. Today*, 1980, **33**(11), 27–33.
2 M. H. Vos, F. Rappaport, J.-C. Lambry, J. Breton and J.-L. Martin, Visualization of coherent nuclear motion in a membrane protein by femtosecond spectroscopy, *Nature*, 1993, **363**(6427), 320–325.
3 A. H. Zewail, Femtochemistry: Atomic-scale dynamics of the chemical bond, *J. Phys. Chem. A*, 2000, **104**(24), 5660–5694.
4 S. T. Park, J. S. Feenstra and A. H. Zewail, Ultrafast electron diffraction: Excited state structures and chemistries of aromatic carbonyls, *J. Chem. Phys.*, 2006, **124**(17), 174707.
5 M. Zhang, S. Zhang, Y. Xiong, H. Zhang, A. A. Ischenko, O. Vendrell, X. Dong, X. Mu, M. Centurion and H. Xu, Quantum state tomography of molecules by ultrafast diffraction, *Nat. Commun.*, 2021, **12**(1), 5441.
6 J. Marangos, The measurement of ultrafast electronic and structural dynamics with X-rays, *Philos. Trans. R. Soc., A*, 2019, **377**(2145), 20170481.
7 Z. Zhang, K. Tanaka and J.-Q. Yu, Remote site-selective C–H activation directed by a catalytic bifunctional template, *Nature*, 2017, **543**(7646), 538–542.
8 N. Goswami, T. Bhattacharya and D. Maiti, Transient directing ligands for selective metal-catalysed C–H activation, *Nat. Rev. Chem.*, 2021, **5**(9), 646–659.
9 B. Ramadoss, Y. Jin, S. Asako and L. Ilies, Remote steric control for undirected meta-selective C–H activation of arenes, *Science*, 2022, **375**(6581), 658–663.
10 B. M. Trost, The atom economy—a search for synthetic efficiency, *Science*, 1991, **254**(5037), 1471–1477.
11 C. M. Marson, Multicomponent and sequential organocatalytic reactions: diversity with atom-economy and enantiocontrol, *Chem. Soc. Rev.*, 2012, **41**(23), 7712–7722.
12 R. F. Heck and J. Nolley Jr, Palladium-catalyzed vinylic hydrogen substitution reactions with aryl, benzyl, and styryl halides, *J. Org. Chem.*, 1972, **37**(14), 2320–2322.
13 C. C. Johansson Seechurn, M. O. Kitching, T. J. Colacot and V. Snieckus, Palladium-catalyzed cross-coupling: a historical contextual perspective to the 2010 Nobel Prize, *Angew. Chem., Int. Ed.*, 2012, **51**(21), 5062–5085.
14 R. M. Jay, A. Banerjee, T. Leitner, R.-P. Wang, J. Harich, R. Stefanuik, H. Wikmark, M. R. Coates, E. V. Beale and V. Kabanova, Tracking C–H activation with orbital resolution, *Science*, 2023, **380**(6648), 955–960.
15 C.-H. Jun, Transition metal-catalyzed carbon–carbon bond activation, *Chem. Soc. Rev.*, 2004, **33**(9), 610–618.
16 J. M. Mayer, Proton-coupled electron transfer: a reaction chemist's view, *Annu. Rev. Phys. Chem.*, 2004, **55**, 363–390.
17 D. R. Weinberg, C. J. Gagliardi, J. F. Hull, C. F. Murphy, C. A. Kent, B. C. Westlake, A. Paul, D. H. Ess, D. G. McCafferty and T. J. Meyer, Proton-coupled electron transfer, *Chem. Rev.*, 2012, **112**(7), 4016–4093.
18 R. I. Cukier and D. G. Nocera, Proton-coupled electron transfer, *Annu. Rev. Phys. Chem.*, 1998, **49**(1), 337–369.
19 A. Das, A. Jha, R. Gera and J. Dasgupta, Photoinduced charge transfer state probes the dynamic water interaction with metal–organic nanocages, *J. Phys. Chem. C*, 2015, **119**(36), 21234–21242.
20 J. C. Barnes, M. Juricek, N. L. Strutt, M. Frasconi, S. Sampath, M. A. Giesener, P. L. McGrier, C. J. Bruns, C. L. Stern and A. A. Sarjeant, ExBox: a polycyclic aromatic hydrocarbon scavenger, *J. Am. Chem. Soc.*, 2013, **135**(1), 183–192.
21 J. K. Klosterman, M. Iwamura, T. Tahara and M. Fujita, Energy transfer in a mechanically trapped exciplex, *J. Am. Chem. Soc.*, 2009, **131**(27), 9478–9479.
22 A. B. Grommet, M. Feller and R. Klajn, Chemical reactivity under nanoconfinement, *Nat. Nanotechnol.*, 2020, **15**(4), 256–271.
23 D. Roy, S. Paul and J. Dasgupta, Visible light-mediated C (sp 3)–H bond functionalization inside an all-organic nanocavity, *Chem. Commun.*, 2023, **59**(88), 13143–13146.
24 R. Gera, A. Das, A. Jha and J. Dasgupta, Light-induced proton-coupled electron transfer inside a nanocage, *J. Am. Chem. Soc.*, 2014, **136**(45), 15909–15912.
25 D. Roy, K. K. Yadav and J. Dasgupta, Host–Guest Charge-Transfer Mediated Photoredox Catalysis Inside Water-Soluble Nanocages, *Acc. Chem. Res.*, 2025, **58**(16), 2600–2612.
26 A. Das, I. Mandal, R. Venkatramani and J. Dasgupta, Ultrafast photoactivation of C–H bonds inside water-soluble nanocages, *Sci. Adv.*, 2019, **5**(2), eaav4806.
27 S. Hammes-Schiffer, Theory of proton-coupled electron transfer in energy conversion processes, *Acc. Chem. Res.*, 2009, **42**(12), 1881–1889.
28 S. Hammes-Schiffer and A. A. Stuchebrukhov, Theory of coupled electron and proton transfer reactions, *Chem. Rev.*, 2010, **110**(12), 6939–6960.
29 R. Schoenlein, L. Peteanu, R. Mathies and C. Shank, The first step in vision: femtosecond isomerization of rhodopsin, *Science*, 1991, **254**(5030), 412–415.
30 C. Fang, R. R. Frontiera, R. Tran and R. A. Mathies, Mapping GFP structure evolution during proton transfer with femtosecond Raman spectroscopy, *Nature*, 2009, **462**(7270), 200–204.
31 G. Batignani, C. Ferrante and T. Scopigno, Accessing excited state molecular vibrations by femtosecond stimulated Raman spectroscopy, *J. Phys. Chem. Lett.*, 2020, **11**(18), 7805–7813.
32 G. Batignani, E. Mai, G. Fumero, S. Mukamel and T. Scopigno, Absolute excited state molecular geometries revealed by resonance Raman signals, *Nat. Commun.*, 2022, **13**(1), 7770.
33 P. Roy, A. Jha, V. B. Yasarapudi, T. Ram, B. Puttaraju, S. Patil and J. Dasgupta, Ultrafast bridge planarization in donor-π-acceptor copolymers drives intramolecular charge transfer, *Nat. Commun.*, 2017, **8**(1), 1716.
34 F. Provencher, N. Bérubé, A. W. Parker, G. M. Greetham, M. Towrie, C. Hellmann, M. Côté, N. Stingelin, C. Silva and S. C. Hayes, Direct observation of ultrafast long-range charge separation at polymer–fullerene heterojunctions, *Nat. Commun.*, 2014, **5**(1), 4288.

35 A. E. Bragg, W. Yu, J. Zhou and T. Magnanelli, Ultrafast Raman spectroscopy as a probe of local structure and dynamics in photoexcited conjugated materials, *J. Phys. Chem. Lett.*, 2016, **7**(19), 3990–4000.

36 J. Dasgupta, R. R. Frontiera, K. C. Taylor, J. C. Lagarias and R. A. Mathies, Ultrafast excited-state isomerization in phytochrome revealed by femtosecond stimulated Raman spectroscopy, *Proc. Natl. Acad. Sci. U. S. A.*, 2009, **106**(6), 1784–1789.

37 B. G. Oscar, C. Chen, W. Liu, L. Zhu and C. Fang, Dynamic Raman line shapes on an evolving excited-state landscape: Insights from tunable femtosecond stimulated Raman spectroscopy, *J. Phys. Chem. A*, 2017, **121**(29), 5428–5441.

38 M. A. Taylor, L. Zhu, N. D. Rozanov, K. T. Stout, C. Chen and C. Fang, Delayed vibrational modulation of the solvated GFP chromophore into a conical intersection, *Phys. Chem. Chem. Phys.*, 2019, **21**(19), 9728–9739.

39 P. Kukura, D. W. McCamant and R. A. Mathies, Femtosecond stimulated Raman spectroscopy, *Annu. Rev. Phys. Chem.*, 2007, **58**, 461–488.

40 R. C. So and A. C. Carreon-Asok, Molecular design, synthetic strategies, and applications of cationic polythiophenes, *Chem. Rev.*, 2019, **119**(21), 11442–11509.

41 S. Flammini, M. Di Sante, P. E. Costantini, E. J. Mattioli, A. Marconi, E. Turrini, S. La Rosa, M. Montrone, T. D. Marforio and M. Nigro, Oligothiophene-based photosensitizers with tunable push–pull architectures: design, synthesis and characterization, *J. Mater. Chem. B*, 2025, **13**(39), 12536–12545.

42 M. Fujita, D. Oguro, M. Miyazawa, H. Oka, K. Yamaguchi and K. Ogura, Self-assembly of ten molecules into nanometre-sized organic host frameworks, *Nature*, 1995, **378**(6556), 469–471.

43 T. J. Wallace and F. A. Baron, Solvent Effects in the Oxidation of Sulfur Compounds. The Base-Catalyzed Oxidation of Alkylthiophenes, *J. Org. Chem.*, 1965, **30**(10), 3520–3523.

44 W. J. KING and F. Nord, PREPARATION OF THIOPHENE-2-ALDEHYDE AND SOME SUBSTITUTED THIOPHENE ALDEHYDES1, *J. Org. Chem.*, 1948, **13**(5), 635–640.

45 W. J. KING and F. Nord, STUDIES IN THE THIOPHENE SERIES. V. WOLFF-KISHNER REDUCTIONS1, 2, *J. Org. Chem.*, 1949, **14**(4), 638–642.

46 Y. Furutani, H. Kandori, M. Kawano, K. Nakabayashi, M. Yoshizawa and M. Fujita, In situ spectroscopic, electrochemical, and theoretical studies of the photoinduced host–guest electron transfer that precedes unusual host-mediated alkane photooxidation, *J. Am. Chem. Soc.*, 2009, **131**(13), 4764–4768.

47 T. Keszthelyi, M. M.-L. Grage, J. F. Offersgaard, R. Wilbrandt, C. Svendsen, O. S. Mortensen, J. K. Pedersen and H. J. A. Jensen, 2, 2 '-Bithiophene Radical Cation: An Experimental and Computational Study, *J. Phys. Chem. A*, 2000, **104**(12), 2808–2823.

48 M. M.-L. Grage, T. Keszthelyi, J. F. Offersgaard and R. Wilbrandt, Bithiophene radical cation: resonance Raman spectroscopy and molecular orbital calculations, *Chem. Phys. Lett.*, 1998, **282**(2), 171–175.

49 R. Tyburski, T. Liu, S. D. Glover and L. Hammarström, Proton-coupled electron transfer guidelines, fair and square, *J. Am. Chem. Soc.*, 2021, **143**(2), 560–576.

50 G. J. Zhao, R. K. Chen, M. T. Sun, J. Y. Liu, G. Y. Li, Y. L. Gao, K. L. Han, X. C. Yang and L. Sun, Photoinduced Intramolecular Charge Transfer and S2 Fluorescence in Thiophene-π-Conjugated Donor–Acceptor Systems: Experimental and TDDFT Studies, *Chem.–Eur. J.*, 2008, **14**(23), 6935–6947.

51 Y. Yoneda, S. J. Mora, J. Shee, B. L. Wadsworth, E. A. Arsenault, D. Hait, G. Kodis, D. Gust, G. F. Moore and A. L. Moore, Electron–nuclear dynamics accompanying proton-coupled electron transfer, *J. Am. Chem. Soc.*, 2021, **143**(8), 3104–3112.

52 G. A. Parada, Z. K. Goldsmith, S. Kolmar, B. Pettersson Rimgard, B. Q. Mercado, L. Hammarström, S. Hammes-Schiffer and J. M. Mayer, Concerted proton-electron transfer reactions in the Marcus inverted region, *Science*, 2019, **364**(6439), 471–475.

53 M. H. Shaw, J. Twilton and D. W. MacMillan, Photoredox catalysis in organic chemistry, *J. Org. Chem.*, 2016, **81**(16), 6898–6926.